PAPER

Perpendicular magnetic anisotropy induced by La$_{2/3}$Sr$_{1/3}$MnO$_3$–YBaCo$_2$O$_{5+\delta}$ interlayer coupling

View the article online for updates and enhancements.

Perpendicular magnetic anisotropy induced by La$_{2/3}$Sr$_{1/3}$MnO$_3$–YBaCo$_2$O$_{5+\delta}$ interlayer coupling

Furong Han[1,2], Xiaobing Chen[1,2], Jianlin Wang[1,2], Xudan Huang[1,2], Jine Zhang[1,2], Jinghua Song[1,2], Banggui Liu[1,2] , Yuansha Chen[1,2,5], Xuedong Bai[1,2], Fengxia Hu[1,2,3], Baogen Shen[1,2,3] and Jirong Sun[1,2,3,4]

[1] Beijing National Laboratory for Condensed Matter Physics & Institute of Physics, Chinese Academy of Sciences, Beijing 100190, People's Republic of China
[2] School of Physical Sciences, University of Chinese Academy of Sciences, Beijing 100049, People's Republic of China
[3] Songshan Lake Materials Laboratory, Dongguan, Guangdong 523808, People's Republic of China
[4] Spintronics Institute, University of Jinan, Jinan, Shandong 250022, People's Republic of China
[5] Fujian Innovation Academy, Chinese Academy of Sciences, Fuzhou, Fujian 350108, People's Republic of China

E-mail: yschen@aphy.iphy.ac.cn and jrsun@iphy.ac.cn

CrossMark

Abstract

Heterostructure with a symmetry-mismatched interface provides a promising playground for the exploration of emergent phenomena. Herein, we report a systematic investigation on La$_{2/3}$Sr$_{1/3}$MnO$_3$/YBaCo$_2$O$_{5+\delta}$ (LSMO/YBCO) grown on SrTiO$_3$, a heterostructure formed by perovskite oxides of different symmetry. A high-resolution lattice image shows the formation of high-quality perovskite LSMO and A-site cation-ordered oxygen-deficient double perovskite YBCO, without any signatures of atomic reconfiguration at the interface. Surprisingly, the YBCO-buffered LSMO exhibits perpendicular magnetic anisotropy (PMA), though bare LSMO film is in-plane anisotropic. The PMA is robust, appearing even when the thickness of YBCO is only one unit cell. The typical anisotropy constant is $\sim 4 \times 10^6$ erg cm^{-3}. X-ray absorption spectroscopy analysis reveals a preferential occupation of the $d_{3z^2-r^2}$ orbital compared with $d_{x^2-y^2}$, which is confirmed by density functional theory calculations. This orbital reconstruction accounts for the PMA. The formation of a covalent bond between Mn and Co caged by different oxygen polyhedrons, an octahedron and a square pyramid, respectively, stabilizes the orbital reconstruction, resulting in anomalous spin orientation.

Supplementary material for this article is available online

Keywords: interface, symmetry, magnetic anisotropy, orbital reconstruction, covalent bond

(Some figures may appear in colour only in the online journal)

1. Introduction

Grouping different perovskite oxides into heterostructure opens new avenues for the exploration of emergent phenomena. Due to the interface reconstruction characterized by charge transfer, orbital repopulation and the appearance of chemical bonding across the interface, novel effects are observed, such as the establishment of 2D electron gases

[1–3] and 2D ferromagnetism at the oxide interfaces [4–7], and the alternation of preferred magnetic direction [8–11]. We list just a few examples below. As demonstrated by Liao *et al*, the octahedron rotation transmitted from $NdGaO_3$ to $La_{2/3}Sr_{1/3}MnO_3$ (LSMO) caused anisotropic Mn–O–Mn bond angles along the *a*- and *b*-axes. This in turn results in a switching of the easy magnetic axis of LSMO by an angle of 90° in film plane [9]. As reported by Gibert *et al*, the Mn to Ni charge transfer for $LaMnO_3/LaNiO_3$ heterostructure drives the originally paramagnetic interfacial layer of $LaNiO_3$ into the ferromagnetic state [4]. These are typical effects of the system of perovskite–perovskite combination. Heterostructures with dissimilarly structured oxides also show interesting effects. As reported by Zhang *et al*, perpendicular magnetic anisotropy (PMA) can be achieved by sandwiching the LSMO layer between two brownmillerite $LaCoO_{2.5+\delta}$ layers even when the LSMO layer is in a tensile state that favors in-plane magnetic anisotropy [10]. Further analysis shows that, due to symmetry mismatch, interfacial reconstructions appear, which results in an enhanced elongation of the MnO_6 octahedron, thus, interface orbital reconstruction [12, 13].

Obviously, the heterostructure formed by differently structured oxide provides a promising platform for the exploration of novel effects. Due to the difficulty to get a suitable combination, however, research in this regard is still limited. In this work, we obtained a heterostructure formed by perovskite LSMO and A-site-ordered oxygen-deficient double perovskite $YBaCo_2O_{5+\delta}$ (YBCO) and performed a systematic investigation on the effect of symmetry mismatch. The most remarkable observation is the occurrence of PMA in the YBCO-buffered LSMO, though the bare LSMO film is in-plane anisotropic. The PMA is robust, appearing even when the thickness of YBCO is only one unit cell. X-ray absorption spectroscopy (XAS) analysis and density functional theory (DFT) calculation indicate the occurrence of sizable orbital reconstructions at the interfaces, resulting in anomalous spin orientation.

2. Experimental details

LSMO/YBCO heterostructures were grown on (001)-$SrTiO_3$ (STO) single-crystal substrates ($5 \times 3 \times 0.5$ mm^3) using the technique of pulsed laser deposition (KrF Excimer laser with a wavelength of 248 nm). The deposition sequence is first YBCO, then LSMO layer. During deposition, the oxygen pressure was set to 30 Pa and the substrate temperature was maintained at 800 °C. Here, a slightly high growth temperature was adopted to obtain A-site-ordered double perovskite YBCO. The repetition rate of the laser pulse was 2 Hz and the fluence was 2 J cm^{-2}. After deposition, the samples were cooled to room temperature at a rate of 10 °C min^{-1} in oxygen atmosphere of 100 Pa. The layer thickness was set to 8 uc for YBCO and 9, 18, 31 and 44 uc for LSMO (uc = unit cell). For LSMO = 18 uc, one more sample with only 1 uc thick YBCO was fabricated to explore the ultimate effect of YBCO. The film thickness has been determined by the number of laser pulses, after careful calibration by small-angle x-ray reflectivity technique.

The crystal structure and strain state of the films were determined by a Bruker x-ray diffractometer equipped with thin-film accessories (D8 Discover, Cu Kα radiation). Lattice images were recorded by a high-resolution scanning transmission electron microscope (STEM) with double C_S correctors (JEOL-ARM200F). Magnetic measurements were conducted by a quantum-design vibrating sample magnetometer (VSM-SQUID) in the temperature interval from 5–300 K and the magnetic field range up to 7 T. In the VSM-SQUID, the magnetic field is vertically directed. The sample is mounted on a sample holder so that its surface is parallel or perpendicular to the magnetic field. In this way, the in-plane and out-of-plane magnetic signals were collected. For *M–T* curve, the diamagnetic signal of STO is subtracted as a constant that we get well above the Curie temperature. For *M–H* curve, the diamagnetic signal gives a linear *M–H* curve in the field range well above the saturation field of the sample. We obtained the *M–H* curve of the sample by directly subtracting this linear curve. XAS spectra were collected at the Beamline BL08U1A in the Shanghai Synchrotron Radiation Facility, in total electron yield mode. The XAS spectra were measured around the Mn *L*-edge using two polarized x-ray beams, which form 90° and 30° with the sample plane, respectively, to collect in-plane (E//a, $I_{[001]}$) and out-of-plane (E//c, $I_{[100]}$) signals. The spectra normalization was made by dividing the spectra by a factor so that the L_3 pre-edge and L_2 post-edge have identical intensities for the two polarizations. After that, the pre-edge spectral region was set to zero and the peak at the L_3 edge was normalized to that of the other polarizations. The x-ray linear dichroism (XLD) is calculated as the intensity difference ($I_{[001]−[100]}$) to elucidate Mn 3*d* orbit occupancy.

The DFT calculations were based on the pseudopotential plane-wave method with the projected augmented wave method [14] as implemented in the Vienna *ab initio* simulation package [15, 16]. The generalized gradient approximation of Perdew–Burke–Ernzernhof modified for solids was adopted for exchange-correlation energy [17, 18]. Plane-wave cutoff energy of 600 eV was used. We adopted a *k*-point set generated by the $9 \times 9 \times 3$ Γ-centered mesh for integration over the Brillouin zone [19]. To study the effect of electron correlation, the DFT + *U* approach within the rotationally invariant formalism and the double-counting formula was performed with $U_{\mathrm{eff}} = 6.0$ eV for both Mn and Co 3*d* orbitals. The in-plane lattice constant of the YBCO/LSMO superlattices was fixed at 7.81 Å, which corresponds to the equilibrium lattice constant of STO ($2a_{\mathrm{STO}}$). All internal atomic positions were allowed to fully relax. Atomic positions were optimized until the Hellman–Feynman force on each atom was smaller than 0.01 eV Å^{-1} and the electronic iteration was performed until the total energy change was smaller than 10^{-5} eV.

3. Structure features

LSMO/YBCO heterostructures are coherently grown on substrate, forming high-quality films. Figure 1(a) presents the typical high-angle annular dark-field (HAADF) image of the cross-section of LSMO (18 uc)/YBCO (8 uc), recorded by
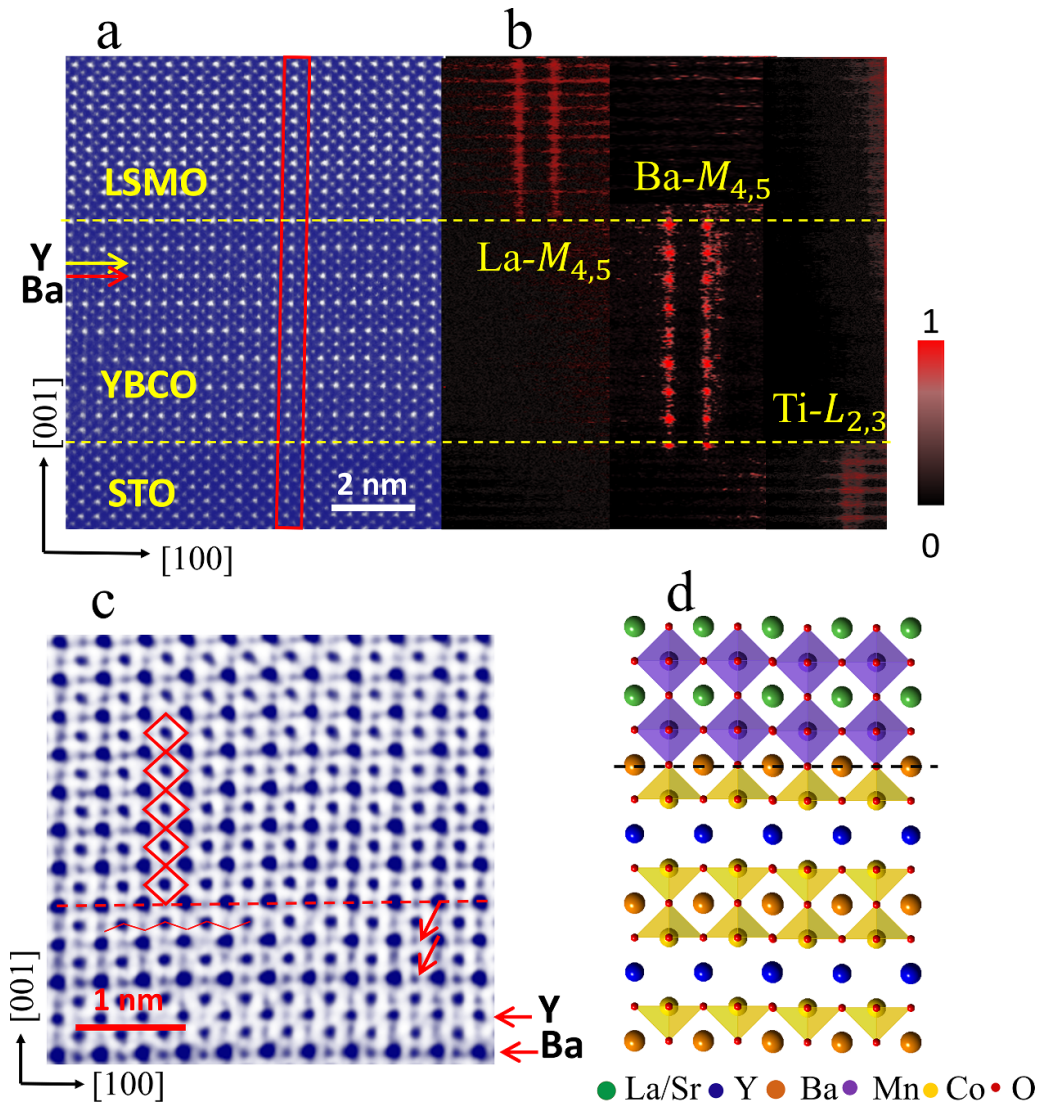
Figure 1. (a) Typical HAADF image of the cross-section of the LSMO (18 uc)/YBCO (8 uc) heterostructure, recorded along the [010] zone axis. Yellow lines mark the LSMO/YBCO and LSMO/STO interfaces. Yellow and red arrow mark the (YO$_\delta$) layer and (BaO) layer, respectively. (b) Corresponding EELS spectrum images of the La-$M_{4,5}$, Ba-$M_{4,5}$ and Ti-$L_{2,3}$ edges, recorded along the vertical red rectangle in (a). Co-$L_{2,3}$ edges are very close to those of Ba-$M_{4,5}$ and are thus not shown. (c) ABF image. Dark dots of the oxygen ion between two horizontally aligned Y ions are much fainter than that between Ba ions. Obviously, this lattice site, which is also the apical oxygen site of the CoO$_6$ octahedron, is less occupied. Dashed line is the LSMO/YBCO interface. Diamonds mark the projection of oxygen octahedron on the *x*–*z* plane. Corrugated line marks the zigzag-shaped Co–O–Co row. Two arrows mark the two oxygen sites between two Y atoms and two Ba atoms, respectively. (d) Sketch of the LSMO/YBCO heterostructure. δ is set to 0 for clarity. Black dashed line marks the LSMO/YBCO interface. MnO$_6$ octahedron and the CoO$_5$ pyramid share apical oxygen at the interface.

STEM along the [010] zone axis. The brightest dot corresponds to Ba. Y is dimmer than Ba but brighter than Co. O atom cannot be recognized. From figures 1(a) and (b), the latter shows the corresponding electron energy loss spectroscopy (EELS) spectrum images recorded along the vertical rectangle in figure 1(a). Two interfaces can be identified (dashed lines in figure 1(a)), separating STO from YBCO and YBCO from LSMO, respectively. The interface is sharp, without visible interlayer diffusion.

As expected, both STO and LSMO are typical perovskite. However, YBCO shows a much more complex structure. At first glance, the Y and Ba layers (marked by yellow and red arrows, respectively) stack alternately along the vertical direction, forming A-site-ordered double perovskite [20–22].

Due to the layer ordering of Ba and Y, the Co–Co separation, calculated along vertical columns, oscillates regularly (not shown). It is long across the Ba layer and short across the Y layer (Ba is bigger than Y in size). This suggests a stacking sequence of (CoO$_2$)–(BaO)–(CoO$_2$)–(YO$_\delta$) along the vertical axis. Here, the notation (YO$_\delta$) is adopted because of the appearance of oxygen vacancies in the (YO) layer. According to the literature, δ generally takes a value between 0.3–0.5 for the experimental conditions similar to ours [20, 21]. As shown by the annular bright-field (ABF) image in figure 1(c), the dark dots of the oxygen ion between two horizontally aligned Y ions are much fainter than that between Ba ions. Obviously, this lattice site, which is also the apical site of the CoO$_6$ octahedron, is less occupied. This in turn causes
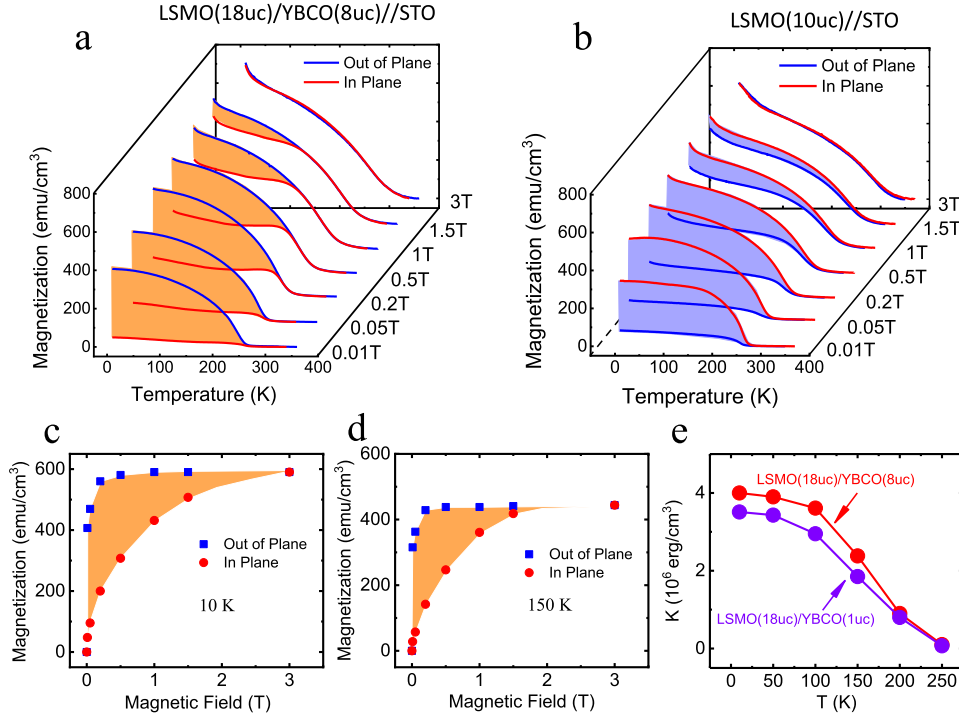
Figure 2. Thermomagnetic curves of LSMO (18 uc)/YBCO (8 uc) heterostructure (a) and bare LSMO (10 uc) film (b), acquired in field-cooling mode with the fields along in-plane and out-of-plane directions, respectively. Shaded areas highlight the magnetic difference of the two measuring directions. (c) and (d) Magnetic moments as functions of magnetic fields applied along two orthogonal directions for LSMO (18 uc)/YBCO (8 uc). Data are extracted from the thermomagnetic curves in (a). (c) $T = 10$ K. (d) $T = 150$ K. Orange area corresponds to the energy required to orient the magnetic moment towards the in-plane direction. (e) Anisotropy constant as a function of temperature. Red and purple curves are the data of the LSMO (18 uc)/YBCO (8 uc) and LSMO (18 uc)/YBCO (1 uc) heterostructures, respectively.

a transition from CoO_6 octahedron to CoO_5 pyramid. Meanwhile, the oxygen atoms just above and below Y go towards Y, forming zigzag-shaped Co–O–Co rows, as marked by the corrugated line [23]. These are typical features of the A-site-ordered oxygen-deficient double perovskite. One more feature that deserves special attention is that the terminal layer of YBCO is (BaO) layer. This phenomenon is also observed in LSMO (18 uc)/YBCO (1 uc), as will be shown later.

Based on these results, a sketch as shown in figure 1(d), can be obtained for the LSMO/YBCO heterostructure. Here, all Co polygons are represented by CoO_5 square pyramids for simplicity. The interface is distinct. It forms between a standard perovskite and an A-site-ordered oxygen-deficient double perovskite. As a consequence, the interfacial MnO_6 octahedron has to share apical oxygen with the CoO_5 square pyramid, which has a completely different orbital configuration to the MnO_6 octahedron. For the standard $YBaCo_2O_5$ structure shown as figure 1(d), there is no oxygen between two adjacent Y atoms. As a result, only CoO_5–MnO_6 pairs exist at the LSMO/$YBaCo_2O_5$ interface, i.e. $\delta = 0$. However, the STEM image shows that the lattice site between two Y sites is partially filled by oxygen, forming the (YO_δ) layer. Therefore, not only CoO_5 pyramids, but CoO_6 octahedrons exist, that is, the LSMO/YBCO interface is formed by $(1-\delta)$ CoO_5–MnO_6 pairs and δ CoO_6–MnO_6 pairs. For example, if $\delta = 0.3$, the CoO_5–MnO_6 pairs at the interface will be 70%.

4. Magnetic behavior

Figure 2(a) shows the magnetization of the heterostructure as a function of temperature (M–T), measured under different magnetic fields (H). The sample behaves differently when applying a magnetic field along film plane and film normal. Along film normal, the typical paramagnetic to ferromagnetic transition at the Curie temperature (T_C) is observed. Along film plane, in contrast, the M–T curve is flat when the field is low and exhibits a slight growth in magnetization around T_C when the field is high. However, the in-plane M–T curves are always lower than those gained using out-of-plane fields until the magnetic field approaches 3 T.

As reported, $YBCO_{5+\delta}$ is antiferromagnetic for $\delta = 0.5$ and weak ferromagnetic when δ deviates from 0.5 [21, 24]. In general, the magnetization of YBCO is generally one order of magnitude lower than that of LSMO, i.e. the magnetic signals of the heterostructure mainly come from LSMO. Therefore, the above results indicate a PMA of the LSMO film in the heterostructure. This is in sharp contrast to bare LSMO film. As is well established, an LSMO film grown on STO is in a tensile state ($a = 3.868$ Å for LSMO and 3.905 Å for STO) and thus exhibits an in-plane easy axis [25, 26]. This conclusion is confirmed by our experiment results for a bare LSMO/STO film (figure 2(b)). The LSMO/YBCO heterostructure grown on (110)-oriented STO substrate does not show PMA according to our experimental results (figure S1

(available online at stacks.iop.org/JPD/54/185302/mmedia) of supplementary materials). In this case, the easy magnetization direction changes to the [1$\bar{1}$0] direction in plane while the bare (110) LSMO is [001] directed (notably, both [1$\bar{1}$0] and [001] are in-plane directions). Fascinatingly, the YBCO buffer layer causes a magnetic reorientation of LSMO.

To get a quantitative description for magnetic anisotropy, anisotropic constant K is calculated. Figures 2(c) and (d) present two typical M–H curves extracted from the M–T curves in figure 2(a), corresponding to two representative temperatures of 10 and 150 K, respectively. When measured along the out-of-plane direction, the sample acquires magnetic saturation at very low fields ($\sim$0.2 T) and the further increase of magnetic field only causes minor variations in magnetization. Along the in-plane direction, in contrast, the saturation state is not gained until the field approaches 3 T for $T = 10$ K and 1.5 T for $T = 150$ K. In fact, anisotropic constant is the energy required to align magnetic moment along a hard axis. It is measured by the area encircled by the in-plane and out-of-plane M–H curves. Direct calculation outputs $K = 4 \times 10^6$ erg cm^{-3} at 10 K and 2.3 $\times 10^6$ erg cm^{-3} at 150 K. The positive sign of K indicates PMA. Notably, this value is comparable to that obtained by Zhang *et al* for a perovskite/brownmillerite interface [10], though the interface here seems to be less asymmetric. K is temperature dependent, due to the variation of magnetization with temperature (figure 2(e)). PMA is also observed when directly measuring M–H loops (figure S2 of supplementary materials). The results of M–H hysteresis are consistent with the conclusion drawn from M–T curves.

The PMA observed here is an interfacial effect, as suggested by the thickness effect of the heterostructures. In figure 3(a), we show the M–T curves for the samples with different LSMO layers collected in a field of 0.05 T, which is applied along film plane or film normal. As expected, all samples show an easy axis along film normal. This feature is especially obvious for the sample with an 18 uc thick LSMO layer, where the discrepancy of the two-direction M–T curves is largest. With the increase of film thickness, the difference between these two M–T curves becomes small, but remains substantial. M–T curves under higher fields were also measured to deduce anisotropy constant (not shown). Based on these data, the K-1/t_{LSMO} relation can be obtained, which is shown in figure 3(b). It is linear for $t_{LSMO} = 18, 31, 44$ uc. This result indicates that the PMA indeed stems from the interface effect [27]. Notably, the *y*-axis interception is negative. This is plausible; when the LSMO in the heterostructure is thick enough, its behavior will be close to that of a bare LSMO that has an in-plane easy axis (negative K). As for the deviation from linearity at $t_{LSMO} = 9$ uc, it is a consequence of magnetic degeneration of the ultrathin LSMO layer. As reported, the magnetic dead layer in LSMO is close to 8 uc in thickness [28].

Further investigation indicates that the PMA of the LSMO is very susceptible to YBCO and a YBCO layer of one unit cell is enough to induce the PMA. Figure 4(a) is the HAADF image of LSMO (18 uc)/YBCO (1 uc), recorded along the [010] zone axis. From figure 4(a) the thickness of the YBCO buffer layer can be determined. It is indeed one unit cell in

LSMO(t_{LSMO})/YBCO(8 uc)//STO
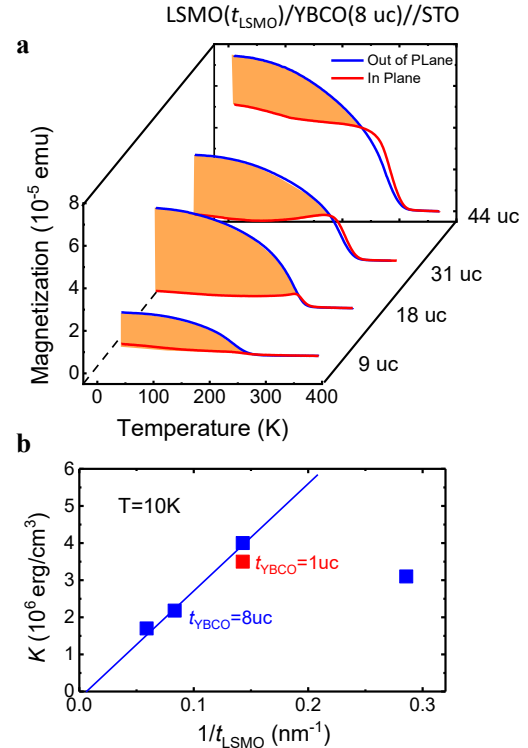
Figure 3. (a) Thermomagnetic curves of the LSMO (t_{LSMO})/YBCO (8 uc) heterostructure, collected in field-cooling mode with an in-plane and out-of-plane applied field of 0.05 T, respectively. Shaded area corresponds to the energy required to orient magnetic moment to the hard axis. (b) Magnetic anisotropy energy as a function of the reciprocal layer thickness of LSMO when YBCO is 8 uc. For comparison, the data for 1 uc thick heterostructure are also shown.

thickness (marked by a yellow rectangle). Figure 4(b) presents the corresponding thermomagnetic curves measured following the same procedure described above. Notably, the out-of-plane direction is the easy magnetic axis, which is the same as the sample with an 8 uc thick YBCO buffer layer. The deduced K-T relation is shown in figure 2(e). It is very close to that of LSMO (18 uc)/YBCO (8 uc). Take the anisotropy constant at 10 K as an example. K is $\sim$4 $\times 10^6$ erg cm^{-3} for LSMO (18 uc)/YBCO (8 uc) and $\sim$3.5 $\times 10^6$ erg cm^{-3} for LSMO (18 uc)/YBCO (1 uc) (figure 3(b)). The strong PMA of LSMO, which will benefit the designing of perovskite-based devices, is an amazing effect of YBCO on LSMO.

It can be seen that there is a crossover between the in-plane and out-of-plane M–T curves, which is more obvious in the case with higher LSMO thickness (figure 3(a)) or higher magnitude of measuring magnetic field (figure 4(b)). We consider that this crossover stems from the competition of several energy terms, such as the magneto-crystalline anisotropy energy, magneto-elastic energy, demagnetizing energy and interface coupling energy introduced by the LSMO/YBCO heterostructure. The crossover is a common phenomenon for all LSMO/YBCO heterostructure samples. Obviously, the interface coupling energy, which turns the magnetic easy axis to the out-of-plane direction, is much more important in thin LSMO films. So, the crossover moves to high temperatures
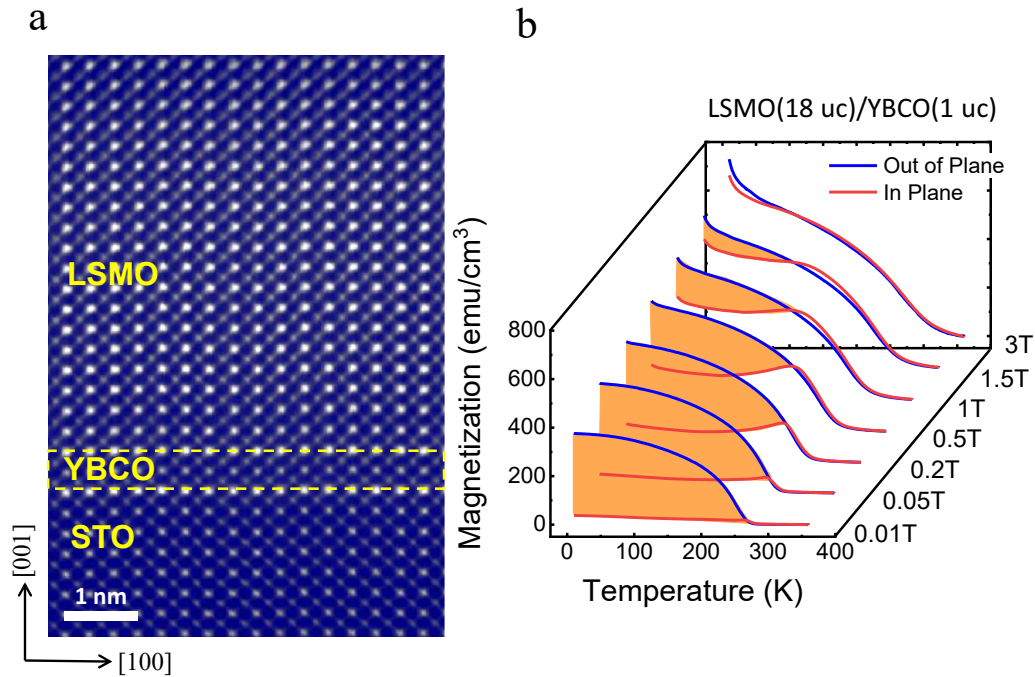
Figure 4. (a) HAADF image of the LSMO (18 uc)/YBCO (1 uc) heterostructure, recorded along the [010] zone axis. Yellow rectangle marks the YBCO layer. (b) Corresponding thermomagnetic curves, acquired in field-cooling mode with the fields along the in-plane and out-of-plane directions, respectively.

for this kind of heterostructure, which can be clearly seen in the *M–T* curves. In addition, a high magnetic field will overcome the weak PMA, causing the crossover to move to low temperatures.

5. X-ray absorption spectroscopy

According to the Bruno model, the easy magnetic direction has a larger orbital moment than hard magnetic direction [29, 30]. For LSMO, the orbital moment is closely related to orbital populations. To reveal the mechanism of the PMA, we need to know the relative occupations of the two e_g orbits ($d_{3z^2-r^2}$ and $d_{x^2-y^2}$) of Mn, which are not degenerate due to the Jahn–Teller effect and lattice strains [31, 32]. To get the information on orbital structure, the XAS technique was adopted. Figure 5(a) presents the Mn-XAS spectra of the LSMO (18 uc)/YBCO (8 uc) heterostructure. Normalized XAS spectra were recorded with the optical polarizations parallel (E//a, $I_{[100]}$) and perpendicular (E//c, $I_{[001]}$) to the film plane, respectively, where $I_{[100]}$ and $I_{[001]}$ are spectrum intensities in corresponding directions. To highlight the difference in the absorption peaks along two directions, XLD spectra, defined by $I_{[001]}-I_{[100]}$, are calculated. As is well documented, the integration of the XLD spectrum around the L_2 absorption peak gives a direct measure to the occupancy of the $d_{x^2-y^2}$ and $d_{3z^2-r^2}$ orbital states [33, 34]; negative (positive) value means a preferential occupation of the $d_{3z^2-r^2}$ and ($d_{x^2-y^2}$) orbital because the XAS spectra deliver information on empty Mn-3d states [35, 36]. For LSMO (18 uc)/YBCO (8 uc), the XLD spectrum exhibits a negative peak around L_2 (bottom panel of figure 5(a)), indicating that

$d_{3z^2-r^2}$ is the low-lying orbit. A direct calculation shows that, in this case, the orbital moment will align along film normal, which explains the PMA of the heterostructure. The XLD spectrum of LSMO (18 uc)/YBCO (1 uc) shown in figure S3 exhibits a negative peak around the L_2 edge, which is roughly consistent with the LSMO (18 uc)/YBCO (8 uc) heterostructure. The XAS and XLD spectra of the bare LSMO (10 uc)/STO film are also collected for comparison (figure 5(b)). As expected, the XLD spectrum exhibits a positive peak around L_2, i.e. the preferentially occupied orbit now is $d_{x^2-y^2}$. This interprets the in-plane anisotropy of bare LSMO film [36, 37].

6. DFT calculations

The LSMO/YBCO interface in our heterostructures has shown robust PMA and unique orbital reconstruction. To gain further insight into the anomalous phenomenon, DFT calculations have been performed. A simplified structural model is shown in figure 6(a), where the LSMO (2 uc)/YBCO (1 uc) superlattice for $\delta = 0$ was selected for the DFT calculations. YBaCo$_2$O$_5$ contains half Co^{3+} and half Co^{2+}. There is no obvious lattice distortion in the structure after calculation, which is consistent with the ABF image (figure 1(c)). The orbital-resolved density of Mn^{3+} $3d-e_g$ states connected with Co^{2+} or Co^{3+} is shown in figure 6(b) top panel and bottom panel, respectively. A direct calculation yields an occupancy ratio of 1.17:1 for the $d_{x^2-y^2}$ and $d_{3z^2-r^2}$ orbitals when Mn^{3+} connected with Co^{2+}, which stabilizes the magnetization in plane. However, the occupancy ratio becomes
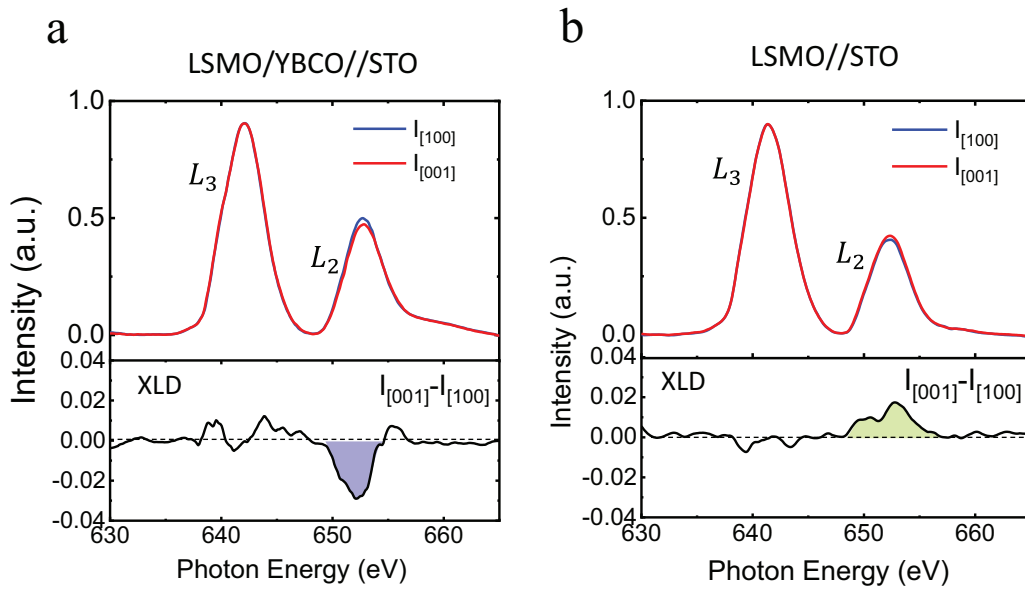
Figure 5. Normalized XAS spectra for (a) LSMO (18 uc)/YBCO (8 uc) heterostructure and (b) bare LSMO (10 uc) film, measured with the optical polarization parallel to the in-plane and out-of-plane direction, respectively. Bottom panels are the corresponding XLD spectra. Its integration over the energy range from 648–660 eV (around the L_2 edge) gives a negative (positive) value, indicating a preferential occupation of the $d_{3z^2-r^2}$ ($d_{x^2-y^2}$) orbital.
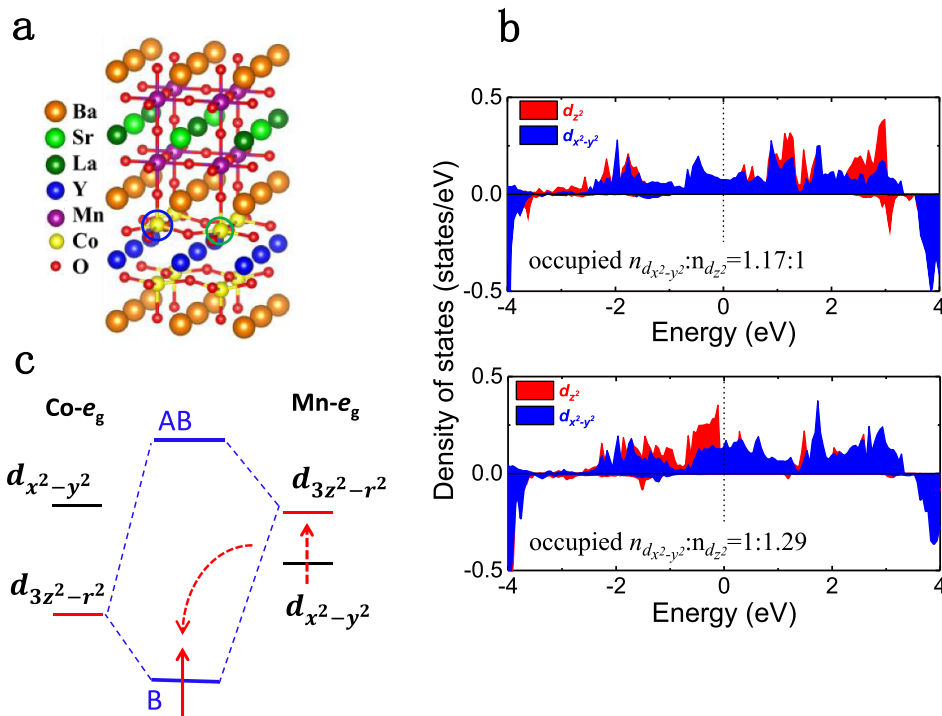
Figure 6. (a) Structural model for DFT calculations, in which the YBaCo$_2$O$_5$ contains half Co^{3+} (in the green circle) and half Co^{2+} (in the blue circle). (b) Projected density of Mn^{3+} $3d-e_g$ states connected with Co^{2+} (top panel) or Co^{3+} (bottom panel). $d_{3z^2-r^2}$ and $d_{x^2-y^2}$ states are marked in red and blue colors, respectively. (c) Sketch illustrating the bonding (B) and anti-bonding (AB) states of the $d_{3z^2-r^2}$ orbits of the 3d electrons of Mn and Co caged by oxygen octahedron and pyramid, respectively. Low-lying $d_{3z^2-r^2}$ level of CoO$_5$ pulls down the $d_{3z^2-r^2}$ level of MnO$_6$ greatly after chemical bonding, resulting in preferential occupation of the $d_{3z^2-r^2}$ state.

1:1.29 for the $d_{x^2-y^2}$ and $d_{3z^2-r^2}$ orbitals when Mn^{3+} connected with Co^{3+}. This implies an orbital reconstruction that causes a low-level shift of $d_{3z^2-r^2}$ with respect to $d_{x^2-y^2}$. Usually, the Y^{3+} ions, Ba^{2+} ions and O^{2-} ions are invariable.

Therefore, the mean valence state of Co ions in the YBaCo$_2$O$_5$ structure is 2.5+, which means half Co^{3+} and half Co^{2+}. For the YBCO phase, after simple calculation, the content of Co^{3+} ions should be $(1 + 2\delta)/2$. In two special cases of $\delta = 0$

and 0.5, the content of Co^{3+} will be 50% and 1, respectively. Generally speaking, $d_{3z^2-r^2}$ is the preferentially occupied orbit. This result qualitatively agrees with that of the XLD analysis.

7. Discussion

There are intensive investigations on the effect of interface reconstruction on the magnetic properties of perovskite heterostructures. Liao *et al* reported that growing LSMO film on NGO (110) will result in a tilting of the oxygen octahedron near the interface [9]. This in turn leads to in-plane switching of the magnetic easy axis by 90°. In addition, by tuning oxygen octahedron, Kan *et al* realized an in-plane 45° rotation of the easy axis of the SrRuO₃ film [38]. In addition to the work on perovskite–perovskite interface [39–41], there are attempts to fabricate symmetry-mismatch heterostructure to highlight the interface effect. By grouping LSMO and $LaCoO_{2.5+\delta}$ to form a perovskite-brownmillerite heterostructure, Zhang *et al* obtained strong PMA in LSMO that is in the tensile state [10]. The tetrahedral layer of the brownmillerite phase provides space for the distortion of the interfacial MnO_6 octahedron of LSMO, resulting in strong orbital reconstruction, and thus, spin reorientation. It is easy to see that easy axis changes always accompany interface reconstruction.

A remarkable observation of the present work is the change of easy axis without interface reconstruction, though LSMO and YBCO are different in structure. A close inspection of the ABF image around the LSMO/YBCO interface shows that the MnO_6 polygon in LSMO remains perfectly octahedral even when it locates at the LSMO/YBCO interface, without any signatures of tilting/rotating. At first glance (figure 1(c)), the local atomic configuration around the apical oxygen shared by MnO_6 and CoO_5 remains unaffected by the drop of the bottom apical oxygen of CoO_6 and, as a result, no significant atomic rearrangement is required at the interface. As is well known, LSMO grown on STO is a tensile film and shows in-plane magnetic anisotropy because the $d_{x^2-y^2}$ orbit is more preferentially populated than $d_{3z^2-r^2}$. As evidenced by the data of x-ray diffraction (not shown), the YBCO buffer layer does not result in lattice relaxation. It is therefore an interesting question how the orbital reconstruction occurs for LSMO/YBCO.

In previous investigations, an often overlooked effect is chemical bonding [42–45]. In principle, a Co–O–Mn covalent bond will be formed across the interface of the (001) LSMO/YBCO heterostructure; Mn and Co $3d_{3z^2-r^2}$ orbits interact with each other via their overlap with the O $2p_z$ orbit. This in turn causes a downward shift of the $d_{3z^2-r^2}$ orbit [46, 47]. When this effect is strong, the energy level of $d_{x^2-y^2}$ and $d_{3z^2-r^2}$ could be reversed, causing a switching of magnetic anisotropy. This could be the process occurring in the (001) LSMO/YBCO films. Notably, at the interface, MnO_6 octahedra have the opportunity to share apical oxygen with the CoO_5 pyramid. However, due to the absence of apical oxygen, the $d_{3z^2-r^2}$ orbit of CoO_5 has a very low energy level [48].

Consequently, the effect of chemical bonding is particularly strong. It yields a state with $d_{3z^2-r^2}$ character at an energy level that is even lower than the $d_{3z^2-r^2}$ orbit of CoO_5. For the sake of easy understanding, in figure 6(c) we present a sketch illustrating the concept of bonding and anti-bonding states in a molecular orbit picture and also the corresponding energy level configuration. Differently, for the (110) films, the Mn and Co $d_{3z^2-r^2}$ orbitals lie in the film plane that cannot interact with each other. Instead, the Mn $d_{x^2-y^2}$ orbitals will have overlaps with those of the neighboring Co ions via intermediate O $2p_x$ and $2p_y$ orbitals, which form a 45° angle with the film plane. Obviously, this bonding process does not lead to PMA, but only changes the direction of the in-plane anisotropy.

Notably, the bonding effect may not be limited to the interfacial layer. As is well established, double exchange as the dominant mechanism mediates the magnetic exchange among Mn ions in LSMO. However, chemical bonding at the LSMO/YBCO interface stops this process, suppressing the double exchange in the LSMO layers near the interface. This explains the appearance of the PMA in the LSMO film with a finite thickness.

8. Conclusion

We obtained a heterostructure formed by perovskite LSMO and A-site-ordered oxygen-deficient double perovskite YBCO and performed a systematic investigation on the effect of symmetry mismatch. A high-resolution lattice image shows the formation of a high-quality interface, without any signatures of atomic reconfiguration at the interface. The YBCO-buffered LSMO exhibits PMA, though bare LSMO film is in-plane anisotropic. XAS analysis reveals preferential occupation of the $d_{3z^2-r^2}$ orbital rather than $d_{x^2-y^2}$, supporting PMA. The PMA is robust, even appearing when the thickness of YBCO is one unit cell. The typical anisotropy constant is $\sim 4 \times 10^6$ erg cm^{-3}. The results of DFT calculations confirm the orbital reconstruction at the interface, which is consistent with the XAS analysis. The formation of a covalent bond between Mn and Co caged by different oxygen polyhedrons, an octahedron and a square pyramid, respectively, stabilizes the orbital reconstruction, resulting in anomalous spin orientation. This work demonstrates the abundant effects of symmetry-mismatched interfaces.

Data availability statement

The data that support the findings of this study are available from the corresponding author upon reasonable request.

Acknowledgments

J. Phys. D: Appl. Phys. **54** (2021) 185302

F Han *et al*

Conflict of interest

There are no conflicts of interest to declare.

ORCID iDs

Banggui Liu ⓘ https://orcid.org/0000-0002-6030-6680
Jirong Sun ⓘ https://orcid.org/0000-0003-1238-8770

References

[1] Herranz G *et al* 2007 High mobility in LaAlO$_3$/SrTiO$_3$ heterostructures: origin, dimensionality, and perspectives *Phys. Rev. Lett.* **98** 216803

[2] Ohtomo A and Hwang H Y 2004 A high-mobility electron gas at the LaAlO$_3$/SrTiO$_3$ heterointerface *Nature* **427** 423–6

[3] Thiel S, Hammerl G, Schmehl A, Schneider C W and Mannhart J 2006 Tunable quasi-two-dimensional electron gases in oxide heterostructures *Science* **313** 1942–5

[4] Gibert M, Zubko P, Scherwitzl R, Iniguez J and Triscone J M 2012 Exchange bias in LaNiO$_3$–LaMnO$_3$ superlattices *Nat. Mater.* **11** 195–8

[5] Nichols J *et al* 2016 Emerging magnetism and anomalous Hall effect in iridate-manganite heterostructures *Nat. Commun.* **7** 12721

[6] Garcia-Barriocanal J *et al* 2010 Spin and orbital Ti magnetism at LaMnO$_3$/SrTiO$_3$ interfaces *Nat. Commun.* **1** 1080

[7] Okamoto S and Millis A J 2004 Electronic reconstruction at an interface between a Mott insulator and a band insulator *Nature* **428** 630–3

[8] Yi D *et al* 2017 Tuning perpendicular magnetic anisotropy by oxygen octahedral rotations in (La$_{1-x}$Sr$_x$MnO$_3$)/(SrIrO$_3$) superlattices *Phys. Rev. Lett.* **119** 077201

[9] Liao Z *et al* 2016 Controlled lateral anisotropy in correlated manganite heterostructures by interface-engineered oxygen octahedral coupling *Nat. Mater.* **15** 425

[10] Zhang J *et al* 2018 Symmetry mismatch-driven perpendicular magnetic anisotropy for perovskite/brownmillerite heterostructures *Nat. Commun.* **9** 1923

[11] Tebano A *et al* 2008 Evidence of orbital reconstruction at interfaces in ultrathin La$_{0.67}$Sr$_{0.33}$MnO$_3$ films *Phys. Rev. Lett.* **100** 137401

[12] Chen X, Zhang S, Liu B, Hu F, Shen B and Sun J 2019 Theoretical investigation of magnetic anisotropy at the La$_{0.5}$Sr$_{0.5}$MnO$_3$/LaCoO$_{2.5}$ interface *Phys. Rev. B* **100** 144413

[13] Maignan A, Martin C, Pelloquin D, Nguyen N and Raveau B 1999 Structural and magnetic studies of ordered oxygen-deficient perovskites LnBaCo$_2$O$_{5+\delta}$, closely related to the '112' structure *J. Solid State Chem.* **142** 247–60

[14] Blochl P E 1994 Projector augmented-wave method *Phys. Rev. B* **50** 17953–79

[15] Zhang J *et al* 2019 Perpendicular magnetic anisotropy in La$_{1-x}$Sr$_x$CoO$_{2.5+\delta}$/La$_{2/3}$Sr$_{1/3}$MnO$_3$/La$_{1-x}$Sr$_x$CoO$_{2.5+\delta}$ trilayers ($x = 0.05$–0.5) *Phys. Rev. B* **100** 094432

[16] Kresse G and Hafner J 1993 Abinitio molecular-dynamics for liqiud-metals *Phys. Rev. B* **47** 558–61

[17] Kresse G and Hafner J 1994 *ab-initio* molecular-dynamics simulation of the liquid-metal amorphous-semiconductor transition in germanium *Phys. Rev.* B **49** 14251–69

[18] Perdew J P, Burke K and Ernzerhof M 1996 Generalized gradient approximation made simple *Phys. Rev. Lett.* **77** 3865–8

[19] Perdew J P, Ruzsinszky A, Csonka G I, Vydrov O A, Scuseria G E, Constantin L A, Zhou X and Burke K 2008 Restoring the density-gradient expansion for exchange in solids and surfaces *Phys. Rev. Lett.* **100** 136406

[20] Anisimov V I, Zaanen J and Andersen O K 1991 Band theory and Mott insulators: Hubbard-U instead of Stoner-I *Phys. Rev. B* **44** 943–54

[21] Katayama T, Chikamatsu A, Hirose Y, Minohara M, Kumigashira H, Harayama I, Sekiba D and Hasegawa T 2018 Ferromagnetism with strong magnetocrystalline anisotropy in A-site ordered perovskite YBaCo$_2$O$_6$ epitaxial thin films prepared via wet-chemical topotactic oxidation *J. Mat. Chem.* C **6** 3445–50

[22] Katayama T, Chikamatsu A, Fukumura T and Hasegawa T 2016 Topotactic reductive synthesis of A-site cation-ordered perovskite YBaCo$_2$O$_x$ ($x = 4.5$–5.5) epitaxial thin films *Japan. J. Appl. Phys.* **55** 04EJ05

[23] Lebedev O I, Turner S, Caignaert V, Cherepanov V A and Raveau B 2016 exceptional layered ordering of cobalt and iron in perovskites *Chem. Mater.* **28** 2907–11

[24] Galeano V, Arnache O, Supelano I, Parra Vargas C A and Moran O 2016 Growth and characterization of textured YBaCo$_2$O$_{5+\delta}$ thin films grown on (001)-SrTiO$_3$ via DC magnetron sputtering *Thin Solid Films* **609** 1–5

[25] Tsui F, Smoak M C, Nath T K and Eom C B 2000 Strain-dependent magnetic phase diagram of epitaxial La$_{0.67}$Sr$_{0.33}$MnO$_3$ thin films *Appl. Phys. Lett.* **76** 2421–3

[26] Haghiri-Gosnet A M, Wolfman J, Mercey B, Simon C, Lecoeur P, Korzenski M, Hervieu M, Desfeux R and Baldinozzi G 2000 Microstructure and magnetic properties of strained La$_{0.7}$Sr$_{0.3}$MnO$_3$ thin films *J. Appl. Phys.* **88** 4257–64

[27] Johnson M T, Bloemen P J H, denBroeder F J A and deVries J J 1996 Magnetic anisotropy in metallic multilayers *Rep. Prog. Phys.* **59** 1409–58

[28] Sun J Z, Abraham D W, Rao R A and Eom C B 1999 Thickness-dependent magnetotransport in ultrathin manganite films *Appl. Phys. Lett.* **74** 3017–9

[29] Bruno P 1989 Tight-binding approach to the orbital magnetic-moment and magnetocrystalline anisotropy of transition-metal monolayers *Phys. Rev. B* **39** 865–8

[30] Bruno P 1993 *Magnetismus Von Festkörpern Und Grenzflächen* (Jülich: KFA) ch 24, p 1–p

[31] Fang Z, Solovyev I V and Terakura K 2000 Phase diagram of tetragonal manganites *Phys. Rev. Lett.* **84** 3169–72

[32] Saitoh T, Bocquet A E, Mizokawa T, Namatame H, Fujimori A, Abbate M, Takeda Y and Takano M 1995 Electronic-structure OF La$_{1-x}$Sr$_x$MnO$_3$ studied by photoemission and x-ray-absorption spectroscopy *Phys. Rev. B* **51** 13942–51

[33] Degroot F M F, Fuggle J C, Thole B T and Sawatzky G A 1990 L$_{2,3}$ x-ray-absorption edges of D$_0$ compounds—K$^+$, Ca^{2+}, Sc^{3+} And Ti^{4+} In OH (octahedral) symmetry *Phys. Rev. B* **41** 928–37

[34] Aruta C, Ghiringhelli G, Tebano A, Boggio N G, Brookes N B, Medaglia P G and Balestrino G 2006 Strain induced x-ray absorption linear dichroism in La$_{0.7}$Sr$_{0.3}$MnO$_3$ thin films *Phys. Rev. B* **73** 235121

[35] Huang D J *et al* 2004 Orbital ordering in La$_{0.5}$Sr$_{1.5}$MnO$_4$ studied by soft x-ray linear dichroism *Phys. Rev. Lett.* **92** 087202

J. Phys. D: Appl. Phys. **54** (2021) 185302

F Han *et al*

[36] Huijben M, Martin L W, Chu Y H, Holcomb M B, Yu P, Rijnders G, Blank D H A and Ramesh R 2008 Critical thickness and orbital ordering in ultrathin $La_{0.7}Sr_{0.3}MnO_3$ films *Phys. Rev.* B **78** 094413

[37] Pesquera D, Herranz G, Barla A, Pellegrin E, Bondino F, Magnano E, Sanchez F and Fontcuberta J 2012 Surface symmetry-breaking and strain effects on orbital occupancy in transition metal perovskite epitaxial films *Nat. Commun.* **3** 2189

[38] Kan D, Aso R, Sato R, Haruta M, Kurata H and Shimakawa Y 2016 Tuning magnetic anisotropy by interfacially engineering the oxygen coordination environment in a transition metal oxide *Nat. Mater.* **15** 432

[39] Lin S *et al* 2020 Switching magnetic anisotropy of $SrRuO_3$ by capping-layer-induced octahedral distortion *Phys. Rev. Appl.* **13** 034033

[40] Han F *et al* 2020 Spin reorientation at (110)-$La_{2/3}Sr_{1/3}MnO_3$/$LaCoO_3$ interfaces by orbital/charge reconstruction *APL Mater.* **8** 021113

[41] Zhang J *et al* 2018 Magnetic anisotropy controlled by distinct interfacial lattice distortions at the $La_{1-x}Sr_xCoO_3$/$La_{2/3}Sr_{1/3}MnO_3$ interfaces *ACS Appl. Mater. Interfaces* **10** 40951–7

[42] Cui B, Li F, Song C, Peng J J, Saleem M S, Gu Y D, Li S N, Wang K L and Pan F 2016 Insight into the antiferromagnetic structure manipulated by electronic reconstruction *Phys. Rev.* B **94** 134403

[43] Chakhalian J, Freeland J W, Habermeier H U, Cristiani G, Khaliullin G, van Veenendaal M and Keimer B 2007 Orbital reconstruction and covalent bonding at an oxide interface *Science* **318** 1114–7

[44] Yu P *et al* 2010 Interface ferromagnetism and orbital reconstruction in $BiFeO_3$–$La_{0.7}Sr_{0.3}MnO_3$ heterostructures *Phys. Rev. Lett.* **105** 027201

[45] Mahadevan P, Shanthi N and Sarma D D 1996 Estimates of electronic interaction parameters for $LaMO_3$ compounds (M = Ti-Ni) from *ab initio* approaches *Phys. Rev.* B **54** 11199–206

[46] Cui B, Song C, Gehring G A, Li F, Wang G, Chen C, Peng J, Mao H, Zeng F and Pan F 2015 Electrical manipulation of orbital occupancy and magnetic anisotropy in manganites *Adv. Funct. Mater.* **25** 864–70

[47] Song J *et al* 2020 Electric tuning of magnetic anisotropy and exchange bias of $La_{0.8}Sr_{0.2}CoO_3$/$La_{0.67}Sr_{0.33}MnO_3$ bilayer films *Phys. Rev. Appl.* **14** 024062

[48] Grimaud A, May K J, Carlton C E, Lee Y L, Risch M, Hong W T, Zhou J and Shao-Horn Y 2013 Double perovskites as a family of highly active catalysts for oxygen evolution in alkaline solution *Nat. Commun.* **4** 2439